JOURNAL OF SPACECRAFT AND ROCKETS
Vol. 46, No. 4, July–August 2009

Engineering Note

Constitutive Properties of Silicone-Impregnated Reusable Ceramic Ablator in Compression: Poisson's Ratios

Mike H. B. Gray*
Occidental College, Los Angeles, California 90041
and
Lev Kurbanyan† and Frederick Milstein‡
University of California, Santa Barbara, Santa Barbara, California 93106

DOI: 10.2514/1.34350

Nomenclature

E_B	=	Young's modulus in the bulk, MPa
E_P	=	Young's modulus for parallel loading, MPa
E_T	=	Young's modulus for transverse loading, MPa
e	=	instantaneous strain at a point
e_B	=	instantaneous linear (uniform) strain throughout the bulk
e_S	=	instantaneous nonlinear (nonuniform) strain in the surface layer
L	=	gauge length, mm
L_S	=	effective thickness of the surface layer, mm
L'	=	L/L_S
t	=	sample height or thickness, mm
ε	=	strain measured over a gauge length L
ε_1	=	intrinsic strain measured perpendicular to the preferred plane
ε_2, ε_3	=	intrinsic strain measured parallel to the preferred plane
ε_X	=	intrinsic strain parallel to the applied load
ε_Y	=	intrinsic strain perpendicular to the applied load
ν_{12}	=	Poisson ratio, $-\varepsilon_2/\varepsilon_1$
ν_{21}	=	Poisson ratio, $-\varepsilon_1/\varepsilon_2$
ν_{23}	=	Poisson ratio, $-\varepsilon_3/\varepsilon_2$
ρ	=	density, kg/m^3
σ	=	stress, MPa
σ'	=	σ/E_B

Introduction

THIS paper is the fifth in a series [1–4] of papers that present results of experimental studies, of the mechanical properties of lightweight ceramic ablator (LCA) materials, carried out at the Mechanical Engineering Department at the University of California, Santa Barbara, in support of NASA's space exploration programs. Here we report on measurements of 1) the intrinsic linear elastic compressive response of silicone-impregnated reusable ceramic ablator (SIRCA), from which the Poisson ratios are calculated, and 2) the extrinsic (or global) nonlinear compressive response, which may be reproduced accurately by a theoretical model. The motivation for (and importance of) these mechanical properties studies is discussed in [1,2]. Briefly, LCA materials were developed at the Thermal Protection Materials and Systems Branch at the NASA Ames Research Center for use as heat shields on spacecraft for planetary entry [5–11]. The LCA materials consist of fibrous ceramic substrates that are partially impregnated with organic resins. The fibers in the substrate tend to lie randomly and uniformly parallel to a preferred (unique) plane, hence the LCA materials have complex anisotropic mechanical properties that may be approximated as transversely isotropic, with the unique axis of symmetry perpendicular to the unique plane. The principal types of LCA materials are SIRCA and phenolic impregnated carbon ablator. SIRCA has been used in a number of thermal protection system (TPS) applications, including the successful Mars Pathfinder and Mars Exploration Rover (MER) missions. In particular, SIRCA was used for protection of the parachute deceleration system and the backshell interface plate during entry into the atmosphere of Mars, as well as the transverse impulse rocket system motors, which were employed to reduce lateral landing velocities on Mars.

Parmenter et al. [2] present results of tests of the compressive response of SIRCA; [3] contains results of Iosipescu shear testing of SIRCA and finite element analysis (FEA) modeling of the Iosipescu tests. More recently, while carrying out tests of the mechanical behavior of SIRCA in support of the MER missions, it was found that SIRCA possess a relatively thin, soft, surface layer that can have a profound influence on the overall compressive response; this behavior has been documented in [4]. In particular, Gray and Milstein [4] employed a video microscopy technique to make numerous measurements of stress vs strain in SIRCA samples, over various microscopic gauge lengths L, thereby demonstrating experimentally the existence of SIRCA's soft surface layer. Their experimental stress–strain (σ-ε) responses were recorded over gauge lengths L that both resided within and spanned the softer surface layer. They developed a relatively simple, physically meaningful, analytical model (with but *one* adjustable parameter L_S, the effective thickness of the soft surface layer) to express the nonuniform strain eS, at a point located at a depth x in the soft surface layer, as a function of depth x and level of stress σ, for $0 < x < L_S$. This model enabled them to predict the stress–strain behavior measured over gauges of arbitrary length L (see, e.g., Figs. 2, 3, and 4 in [4]), and which thereby validated the model.

The purpose of our present work is threefold:

1) We report the linear intrinsic compressive stress–strain response (wherein the gauge lengths exclude the softer surface layers) of SIRCA materials; measurements of strain are made simultaneously both parallel and perpendicular to the direction of applied load, from which the intrinsic Poisson ratios are calculated.

2) We compare the linear, intrinsic, compressive stress–strain response of our samples with their nonlinear, extrinsic (or global), compressive response, which is profoundly affected by the soft surface layer, and thereby we point up the importance of distinguishing between mechanical property measurements that include, and those that preclude, the surface layer in their formulation.

3) We review briefly, and suggest a generalization of, the theoretical model developed in [4] to describe the compressive response of SIRCA.

The present tests were carried out on specimens that were not subjected to arc testing, although it may be noted that arc testing affects (i.e., chars) primarily the surface layer of SIRCA and has a much smaller influence upon the interior of the material, and hence

Received 31 August 2007; revision received 15 March 2009; accepted for publication 8 May 2009.

*Adjunct Faculty and Postdoctoral Associate, Chemistry Department; hgray@oxy.edu.

†Student, Mechanical Engineering Department; levkur@engineering.ucsb.edu.

‡Professor, Mechanical Engineering Department and Materials Department; frdmlstn@engineering.ucsb.edu.

may be expected to have a relatively small influence on the intrinsic moduli. Although SIRCA has been used in specific flight testing, there are certainly other potential TPS applications of SIRCA, and to make optimum use of this unique material in any future applications, it will be necessary to determine its full range of mechanical behaviors, many of which have yet to be measured. For example, if SIRCA is bonded to another, stiffer, material and subjected to a compressive load, the ensuing lateral expansions (or the constraint thereof) governed by the Poisson ratios will cause lateral stresses that can cause debonding. Although FEA modeling may be used to analyze such behavior, the Poisson ratios are required for accurate FEA modeling. In the absence of accurate data, overly conservative assumptions need to be put into the FEA analyses which, in turn, may lead to less than optimum deployment.

Methods

Analytical Model

In the model developed by Gray and Milstein [4], a nonuniform strain e at a point located at a position x in the soft surface layer (where x is reckoned from an end of the specimen) depends on position x and level of stress σ; that is, $e = e_S(\sigma, x)$ for $0 < x < L_S$, where L_S is the effective thickness of the soft layer. The stress and strain at any point in the stiffer bulk material are uniform and linearly related; that is, $e = e_B = \sigma/E_B$ for $L_S < x < t - L_S$, where t is the thickness of the specimen and the constant E_B is the intrinsic Young's modulus of the bulk material. Additionally, the strain is assumed to be continuous throughout the material, that is, $e_S(\sigma, L_S) = \sigma/E_B$. Thus, at a given stress, the total strain ε over a gauge length L is given by

$$\varepsilon = \frac{1}{L}\left(\int_0^{L_s} e_s(\sigma, x)\,\mathrm{d}x + \int_{L_s}^{L} e_B(\sigma, x)\,\mathrm{d}x\right) \tag{1}$$

Equation (1) is applicable for cases where the gauge length includes one soft layer and an arbitrary region of the stiffer bulk, that is, where $L_S < L < t - L_S$. If the gauge length lies entirely in the soft layer region, that is, if $L_S > L$, the second integral in Eq. (1) is set to zero and the upper limit on the first integral is set equal to L; if the gauge length spans the full height or thickness of the sample, L in Eq. (1) is set equal to $t/2$, because the strain ε in one-half of the sample (which contains one softer surface layer and one-half of the stiffer bulk) will presumably equal the strain ε in the other half of the sample (which contains the other soft surface layer and the other half of the bulk). In [4], it was shown that excellent agreement between experimental and theoretical compressive stress–strain behavior under parallel compressive loading, for arbitrary gauge lengths, was obtained by use of the function

$$e_s = \left(\frac{\sigma}{E_B}\right)^{x/L_S} \tag{2}$$

which, upon integration of Eq. (1), yielded

$$\varepsilon = \frac{(\sigma' - 1)}{L'\,\ell_n\,\sigma'} + \sigma'\left(1 - \frac{1}{L'}\right) \tag{3}$$

where $L' = L/L_S$ and $\sigma' = \sigma/E_B$.

In Eq. (2), e_S approaches unity as x approaches zero, which implies a vanishing stiffness at the surface; in other words, according to this model, Young's modulus in the soft layer varies rapidly from E_B to zero as x goes from L_S to zero. This loss of stiffness at the surface is seemingly anomalous, or nonphysical, because the material will no doubt possess a finite (nonvanishing, albeit small) stiffness at the surface. The anomaly was explained by Gray and Milstein [4] from the following physical point of view. Given that SIRCA is highly porous [12,13], the modulus becomes extremely small at the very surface of the material owing to the presence of an unfulfilled or open porous structure at the surface, which is much less capable of supporting compressive loads than the interior, closed, porous structure of the material. Equation (2), in which the instantaneous strain e_S approaches unity as x approaches zero, simply reflects the extreme softness at the surface itself. This function thus provides a useful approximation of the response of the material at the surface, because the model is not concerned with strain $e_S(\sigma, 0)$ at the surface per se, but with strain ε over finite gauge lengths L; the strain ε over any finite gauge length of course vanishes as the stress σ approaches zero. Moreover, for compressive loads applied perpendicular to the preferred plane of fiber alignment (i.e., wherein the fibers tend to lie perpendicular to the compressive load), we find that the experimental stress–strain curves have less curvature than the theoretical stress–strain curves based on Eq. (2). This discrepancy suggests that Young's modulus, in the softer surface layers that are parallel to the preferred planes, varies more gradually (from E_B to a noninsignificant finite value) than the variation (from E_B to zero) incorporated in the model strain function of Eq. (2). Thus, we have developed a more general form of the function $e_S(\sigma, x)$, one which will not only be applicable to the case of loading parallel to the preferred plane, but also to the case of loading perpendicular to the preferred plane (and also is more likely to be applicable to porous solids more generally). We do this by setting $x' = x/L_S$ and formulating a Taylor series expansion (about $x' = 1$) of the original function $e_S(\sigma, x)$ given by Eq. (2); this procedure yields

$$e_S(x', \sigma') = \sigma' + \sum_{n=1}^{N} \frac{1}{n!}\sigma'(\ell_n\,\sigma')^n(x' - 1)^n \tag{4}$$

In the limit, as the number of terms N in the summation of Eq. (4) becomes arbitrarily large, Eq. (4) converges to Eq. (2); for any finite value of N, the stiffness at the surface does not vanish, and the smaller the value of the index N, the greater the relative stiffness at the surface (of course, the stiffness is smaller at the surface than anywhere else in the soft layer, except for the case $N = 0$, in which case the summation in Eq. (4) vanishes, along with the softer surface layer, and the material becomes uniformly stiff throughout).

Experimental Procedure

In all of the tests discussed in this paper, a uniform compressive load was applied to cubic samples of SIRCA, 25.4 mm (1.0 in.) on a side, by an Instron 1123 test machine; the load was measured with a precision load cell that is National Institute of Standards and Technology traceable and calibrated to 1% of full scale. The load is applied to one surface of the sample by a flat, rigid steel flange on a moveable crosshead and to the other surface by a "frictionless" steel hemisphere, secured in a lubricated socket on a stationary steel plate. A photograph of the experimental setup is shown in Fig. 1. Within the range of stresses and strains employed in the present study, the specimens did not undergo barreling, and thus potential frictional effects between sample and steel contacts were deemed unimportant. Loads were applied both perpendicular to the preferred plane of fiber orientation (in the 1 direction of Fig. 2), which is referred to as transverse loading, and parallel to the preferred plane (in the 2 or

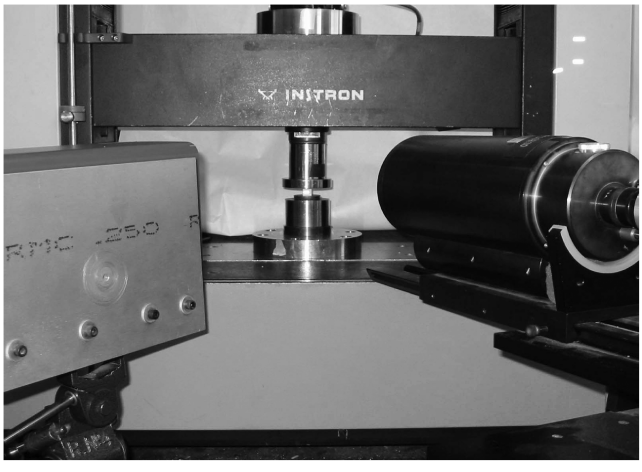

Fig. 1 Photograph of experimental test setup.

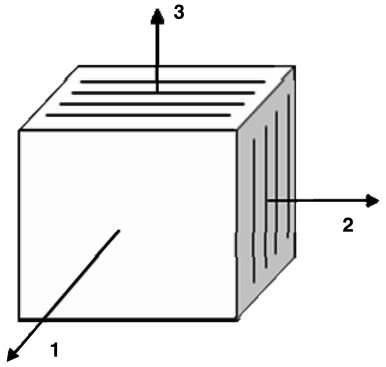

Fig. 2 Illustration of the orthogonal axes by which the Poisson ratios are defined; the 1 axis is perpendicular to the preferred plane of fiber alignment.

3 direction of Fig. 2), which is called parallel loading. The applied stress σ is the axial load divided by the initial cross-sectional area upon which the load acts. Three independent measurements of strain were made continuously and simultaneously while the sample was loaded; strain is defined as the incremental change of a gauge length divided by the initial gauge length. (Here, we define a compressive strain as positive and an expansion as negative.) One of the strain measurements, designated as the global or G measurement, was made with the aid of a linear variable displacement transformer (LVDT) that is internal to the test machine and measures the displacement of the crosshead; the G strain is thus the initial sample thickness (25.4 mm) divided by the displacement of the crosshead. In all of the compression tests, a small preload (of about 1 N or less) was applied to ensure that the sample was under uniform compression before initiating the strain measurements. The preload is also accounted for theoretically by taking a small preload stress and corresponding theoretical preload strain as the origin of the theoretical global stress–strain curves described by Eqs. (1–4), as is discussed in [4]. The intrinsic strains parallel to the load (designated as the X direction) and perpendicular to the load (designated as the Y direction) were made with separate laser extensometers, oriented at 90 deg to each other. Each laser extensometer measured the relative displacement between two small pieces of reflective tape that were adhered to faces of the sample. A micrometer with a resolution of 2.54 μm (0.0001 in.) was used to calibrate the laser extensometers; after calibration of the extensometers, the micrometer and laser measurements agreed to within the level of resolution of the micrometer (i.e., 2.54 μm) under a compression of 0.635 mm (0.025 in.). As a test of the consistency among the LVDT and laser extensometer methods of strain measurement, simultaneous strain measurements were also made on SIRCA specimens over the same gauge lengths, by both methods, as well as by a third method employing video microscopy; these tests yielded excellent agreement among the three methods (as an example, see Fig. 1 in [4]). Because the SIRCA samples are much more compliant than the Instron test machine, there was no need to adjust for any possible error in the G strain measurements owing to possible strain in the Instron during testing, as was verified by the three independent strain measurements.

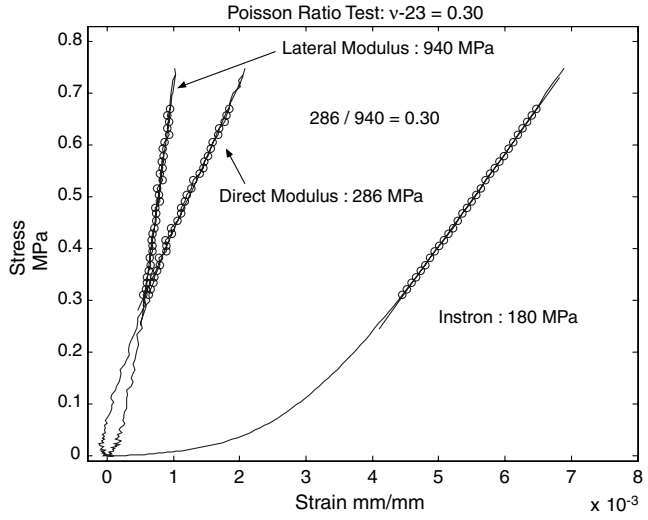

Fig. 3 Examples of data that were sampled for the determination of the Poisson ratios.

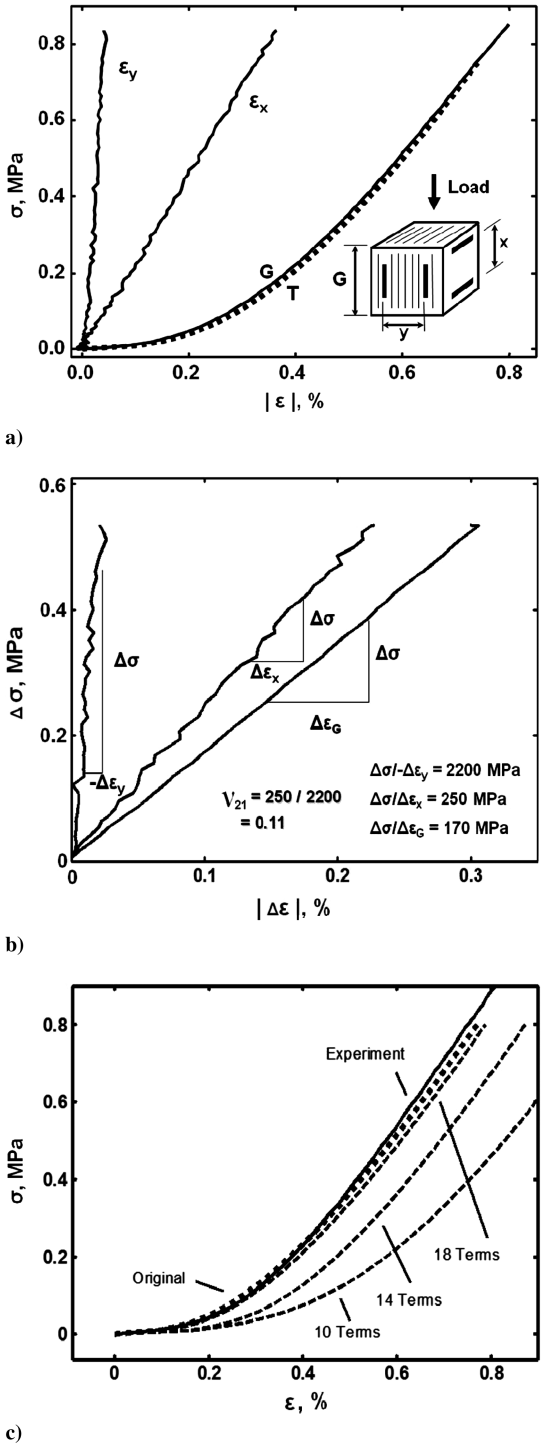

Fig. 4 Parallel loading and measurement of a ν_{21}: a) loading configuration, the intrinsic direct ε_X and lateral ε_Y stress–strain responses employed for determining ν21, and the global experimental G and theoretical T stress-strain responses; b) data from Fig. 4a shown over the range where the G response is essentially linear; c) illustration of the rate of convergence of the theoretical σ-ε relation based on Eq. (4) to that of Eq. (2), as N increases from 10 to 18 terms in the summation of Eq. (4).

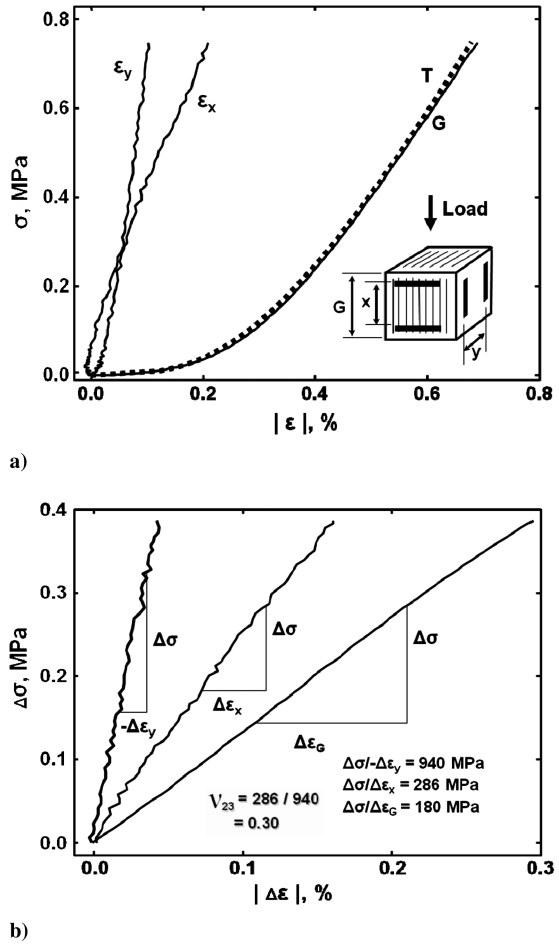

Fig. 5 Parallel loading and measurement of ν_{23}: a) loading configuration, the intrinsic direct ε_X and lateral ε_Y stress–strain responses employed for determining ν_{23}, and the global experimental G and theoretical T stress–strain responses; b) data from Fig. 5a shown over the range where the G response is essentially linear.

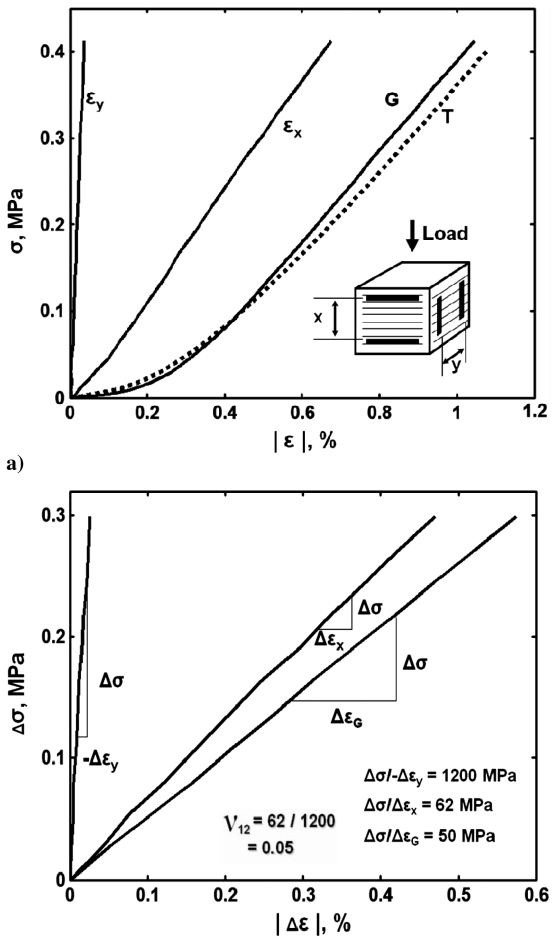

Fig. 6 Transverse loading and measurement of ν_{12}. a) Loading configuration, the intrinsic direct ε_X and lateral ε_Y stress–strain responses employed for determining ν_{12}, and the global experimental G and theoretical T stress–strain responses; b) data from Fig. 6a shown over the range where the G response is essentially linear.

Young's modulus E is defined as the slope of the largest linearly increasing portion of the σ-ε curve. The two independent Young's moduli are designated E_T and E_P, for loads applied perpendicular (or transverse) and parallel to the preferred plane, respectively; thus, E_T is measured under a load parallel to the 1 direction in Fig. 2 and E_P is measured when the load is applied along the 2 or 3 direction in Fig. 2. The strains ε_1, ε_2, and ε_3 are similarly defined as the intrinsic strains in the 1, 2, and 3 directions of Fig. 2. The Poisson ratio is defined as the negative ratio of the lateral strain divided by the direct axial strain, that is, $-\varepsilon_Y/\varepsilon_X$; thus, with respect to the orientation cube of Fig. 2, the three Poisson ratios that were measured in the present study are

$$\nu_{21} = -\frac{\varepsilon_1}{\varepsilon_2} \tag{5}$$

$$\nu_{23} = -\frac{\varepsilon_3}{\varepsilon_2} \tag{6}$$

$$\nu_{12} = -\frac{\varepsilon_2}{\varepsilon_1} \tag{7}$$

Equations (5) and (6) are based on a uniform stress in the 2 direction. Equation (7) is based on a uniform stress in the 1 direction. Although Eqs. (5) and (7) are related by reciprocity, it is important to note that the three Poisson ratios were measured independently. The method of determining the Poisson ratios, as is described in the next section, consisted of taking the ratios of the slopes of two independent, simultaneously measured, stress–strain responses (i.e., for the strains measured both parallel and perpendicular to the applied load). The process consisted of sampling between 30 and 40 sets of data points electronically for each stress–strain response and using the least-squares method to determine the best linear fit to the data (i.e., to determine the slopes of the stress–strain data). The range over which data were sampled was a sufficiently large linear region of the stress–strain response, so that the results converged (with respect to variations in the range of data and the number of data points sampled). Examples of the data points that were sampled are shown in Fig. 3.

Results and Discussion

Figure 4 shows an example of results of a stress–strain test from which a numerical value of ν_{21} was determined; this figure also illustrates the method of determining this Poisson ratio. For measurement of ν_{21}, the load is applied parallel to the 2 axis, the direct intrinsic strain ε_X is identical to ε_2, and the lateral intrinsic strain ε_Y is ε_1; thus, the strips of reflective laser tape that delineate the gauge length for measurements of these strains are placed as is illustrated in the sketch of the cube in Fig. 4a. Figure 4a also shows the corresponding global experimental G and theoretical T stress–strain relations, wherein the theoretical result is based on Eqs. (1–3), with $L_S = 0.610$ mm, $E_B = 250$ MPa, and a preload of 0.0012 MPa. Figure 4b shows the experimental data of Fig. 4a in the range where the G response is essentially linear; that is, the origin of the stress–strain curves in Fig. 4b is taken to be the stress of 0.3 MPa (in Fig. 4a) and the corresponding strains at this stress. For the test represented in Fig. 4, the direct intrinsic modulus $E_P = \Delta\sigma/\Delta\varepsilon_X = 250$ MPa

Table 1 Measurements of Poisson ratio ν_{21} (parallel loading)

Sample	Load no.	Density ρ, kg/m^3	Direct gauge length, mm	Lateral gauge length, mm	Direct modulus E_P, MPa	Lateral modulus, MPa	ν_{21}
1	1	256	19.2	17.8	172	2000	0.09
	2	256	19.2	17.8	193	——	——
	3	256	19.2	17.8	190	1860	0.10
2	1	257	19.7	19.1	223	1400	0.16
	2	257	19.7	19.1	230	1375	0.17
	3	257	19.7	19.1	225	1450	0.16
3	1	257	19.5	19.2	283	——	——
	2	257	19.5	19.2	270	——	——
	3	257	19.5	19.2	265	——	——
	4	257	19.4	18.4	260	1600	0.16
	5	257	19.4	18.4	250	1650	0.15
4	1	258	19.3	17.4	240	——	——
	2	258	19.3	17.4	245	2100	0.12
	3	258	19.3	17.4	250	2200	0.11
	4	258	19.3	17.4	245	——	——
	5	258	19.3	17.4	240	——	——
Average		257	——	——	236	1737	0.14
Standard deviation		0.719	——	——	30.3	313	0.030

Table 2 Measurements of Poisson ratio ν_{23} (parallel loading)

Sample	Load no.	Density ρ, kg/m^3	Direct gauge length, mm	Lateral gauge length, mm	Direct modulus E_P, MPa	Lateral modulus, MPa	ν_{23}
5	1	257	18.7	16.2	220	934	0.24
	2	257	18.7	16.2	215	911	0.24
	3	257	18.6	15.4	240	926	0.26
6	1	260	18.0	17.2	286	940	0.30
	2	260	18.0	17.2	286	980	0.29
	3	260	18.0	16.7	272	990	0.27
Average		259	——	——	253	947	0.27
Standard deviation		1.64	——	——	32.4	31.3	0.025

(which is also the intrinsic modulus E_B, of course) and the lateral intrinsic modulus $\Delta\sigma/(-\Delta\varepsilon_Y) = 170$ MPa; the Poisson ratio ν_{21} is then given by the ratio of the intrinsic lateral modulus to the intrinsic direct modulus. The direct intrinsic modulus is also clearly larger than the apparent global modulus of 170 MPa, owing to the effect of the soft layer on the latter modulus. The triangles that illustrate the Δ stresses and Δ strains in Fig. 4b are for illustrative purposes and are not intended to indicate the range of data that were included in the moduli calculations. Figure 4c illustrates the rate of convergence of the theoretical stress–strain relation based on Eq. (4) to that based on the original function, given by Eq. (2), for the cases of $N = 10$, 14, and 18 terms in the summation of Eq. (4). For $N = 20$ terms, the results based on Eqs. (2) and (4) are essentially indistinguishable. Figures 5a, 5b, 6a, and 6b present examples of data used to determine

Table 3 Measurements of Poisson ratio ν_{12} (transverse loading)

Sample	Load no.	Density ρ, kg/m^3	Direct gauge length, mm	Lateral gauge length, mm	Direct modulus E_P, MPa	Lateral modulus, MPa	ν_{12}
7	1	273	19.9	18.9	76	1630	0.05
	2	273	19.9	18.9	72	1650	0.04
	3	273	19.9	18.9	75	3400	0.02
8	1	265	20.5	18.2	62	1300	0.05
	2	265	20.5	18.2	62	1150	0.05
	3	265	20.5	18.2	62	1200	0.05
	4	265	20.5	18.2	62	1220	0.05
	5	265	20.5	18.2	62	1150	0.05
9	1	263	19.4	17.6	70	776	0.09
	2	263	19.4	17.6	66	1300	0.05
	3	263	19.4	17.6	67	1270	0.05
	4	263	19.4	17.6	66	1300	0.05
10	1	262	19.7	18.9	68	1300	0.05
	2	262	19.7	18.9	66	1100	0.06
	3	262	19.7	18.9	65	1500	0.04
	4	262	19.7	18.9	64	1550	0.04
Average		265	——	——	67	1425	0.05
Standard deviation		4.02	——	——	4.6	570	0.014

numerical values of the Poisson ratios ν_{23} and ν_{12}, respectively, in a format similar to that of Figs. 4a and 4b; the plots and accompanying sketches of the orientation cubes should therefore be self-explanatory in Figs. 5 and 6. In Fig. 5a, the theoretical global stress response is based on Eq. (2), with $L_s = 0.508$ mm, $E_B = 286$ MPa, and a preload of 0.00012 MPa; in Fig. 6a, the theoretical global stress response is based on Eq. (4), with $N = 10$, $Ls = 0.356$ mm, $E_B = 62$ MPa, and the preload $= 0.002$ MPa. The origin for the linear plots in Fig. 5b is 0.3 MPa, as in Fig. 4b, whereas the origin for the linear plots for the data in Fig. 6b is 0.1 MPa (which is the stress at which the transverse global stress–strain plot becomes essentially linear).

Tables 1–3 show the results of tests made on 10 separate samples. Each sample was tested multiple times. The direct and lateral moduli listed in these tables are all intrinsic moduli measured with the laser extensometers. Missing entries for the lateral modulus in Table 1 are a result of experimental uncertainties owing to noise in the data. As would be expected, based upon one's intuition, the direct moduli are larger under parallel loading than under transverse loading, and the Poisson ratios are ordered according to $\nu_{23} > \nu_{21} > \nu_{12}$.

For a purely transversely isotropic material, there are five independent elastic moduli, which may be represented by E_T, E_P, ν_{21} (or ν_{12}), ν_{23} (or G_{23}), and G_{12}, where G_{23} and G_{12} are shear moduli [14]. The Poisson ratios ν_{21} and ν_{12} are related to the Young moduli by the relation

$$\frac{\nu_{21}}{E_P} = \frac{\nu_{12}}{E_T} \tag{8}$$

and the shear modulus G_{23} is related to E_P and ν_{23} by

$$G_{23} = \frac{E_P}{2(1 + \nu_{23})} \tag{9}$$

From the data in Table 1, we find that ν_{21}/E_P is approximately $0.14/236 = 6 \times 10^{-4}$ MPa^{-1}, whereas, from Table 3, we see that ν_{12}/E_T is about $0.05/67 = 7 \times 10^{-4}$ MPa^{-1}, which is in reasonably good agreement with Eq. (8). We are also able to estimate the shear modulus G_{23} from Eq. (9) and the data in Table 2; that is, G_{23} is approximately $253/2(1 + 0.27) = 100$ GPa.

Conclusions

Measurements were made of the two intrinsic Young moduli E_T and E_P and the three Poisson ratios ν_{23}, ν_{21}, and ν_{12} of silicone-impregnated reusable ceramic ablator. The average numerical values of the Poisson ratios were $\nu_{23} = 0.27 \pm 0.025$, $\nu_{21} = 0.14 \pm 0.030$, and $\nu_{12} = 0.05 \pm 0.014$, where the $\pm$ values are 1 standard deviation. The results are in reasonably good agreement with the theoretical relation $\nu_{21}/E_P = \nu_{12}/E_T$ for transversely isotropic materials. Additionally, a model for describing the influence of SIRCA's soft surface layer upon the compressive response was generalized to account for cases in which the Young modulus does not vanish at the surface.

Acknowledgments

This work was supported in part by NASA Grant NCC2-1290. We wish to acknowledge Kirk Fields, Jeffrey Loomis, Mark Newfield, Dan Rasky, and Christine Szalai for their help and encouragement.

References

[1] Parmenter, K. E., Shuman, K., Milstein, F., Szalai, C. E., Tran, H. K., and Rasky, D. J., "Compressive Response of Lightweight Ceramic Ablators: Phenolic Impregnated Carbon Ablator," *Journal of Spacecraft and Rockets*, Vol. 38, No. 2, 2001, pp. 231–236. doi:10.2514/2.3675

[2] Parmenter, K. E., Shuman, K., Milstein, F., Szalai, C. E., Tran, H. K., and Rasky, D. J., "Compressive Response of Lightweight Ceramic Ablators: Silicone Impregnated Reusable Ceramic Ablator," *Journal of Spacecraft and Rockets*, Vol. 39, No. 2, 2002, pp. 290–298. doi:10.2514/2.3811

[3] Nagasawa, S., Parmenter, K. E., Shuman, K., and Milstein, F., "Experimental Failure Modes and FEA of Lightweight Ceramic Ablators under Iosipescu Testing," *Proceedings of the 10th International Congress of Fracture* [CD-ROM], Elsevier, New York, Dec. 2001.

[4] Gray, M. H. B., and Milstein, F., "Methodology for Determining the Influence of Soft Surface Layers in Porous Solids on Compressive Behavior: Application to NASA's Lightweight Ceramic Ablator," *Review of Scientific Instruments*, Vol. 77, No. 2, 2006, pp. 026104-1–26104-4. doi:10.1063/1.2173067

[5] Tran, H. K., "Development of Lightweight Ceramic Ablators and Arc Jet Test Results," NASA TM 108798, 1994.

[6] Tran, H. K., Johnson, C. E., Rasky, D. J., Hui, F. C. L., Chen, Y.-K., and Hsu, M.-T., "Phenolic Impregnated Ablators (PICA) for Discovery Class Missions," AIAA Paper 96-1911, June 1996.

[7] Tran, H. K., Johnson, C. E., Rasky, D. J., Hui, F. C. L., Chen, Y.-K., and Hsu, M.-T., "Silicone Impregnated Reusable Ceramic Ablators for Mars Follow-On Missions," AIAA Paper 96-1819, June 1996.

[8] Tran, H. K., Johnson, C. E., Hsu, M.-T., Smith, M., Dill, H., and Chen-Jonsson, A., "Qualification of the Forebody Heatshield of the Stardust's Sample Return Capsule," AIAA Paper 97-2482, June 1997.

[9] Tran, H. K., Johnson, C. E., Rasky, D. J., Hui, F. C. L., Hsu, M.-T., Chen, T., Chen, K. Y., Paragas, D., and Kobayashi, L., "Phenolic Impregnated Carbon Ablators (PICA) as Thermal Protection Systems for Discovery Missions," NASA TM 110440, April 1997.

[10] Chen, Y.-K., and Milos, F. S., "Ablation and Thermal Response Program for Spacecraft Heatshield Analysis," AIAA Paper 98-0273, Jan. 1998.

[11] Milos, F. S., and Squire, T. H., "Thermostructural Analysis of Silicone Impregnated Reusable Ceramic Ablator Tile for X-34 Wing Leading Edge Thermal protection System," AIAA Paper 98-0883, Jan. 1998.

[12] Marschall, J., and Milos, F. S., "Gas Permeability of Rigid Fibrous Refractory Insulations," *Journal of Thermophysics and Heat Transfer*, Vol. 12, No. 4, 1998, pp. 528–535. doi:10.2514/2.6372

[13] Marschall, J., and Cox, M. E., "Gas Permeability of Lightweight Ceramic Ablators," *Journal of Thermophysics and Heat Transfer*, Vol. 13, No. 3, 1999, pp. 382–384. doi:10.2514/2.6451

[14] Daniel, I. M., and Ishai, O., *Engineering Mechanics of Composite Materials*, Oxford Univ. Press, New York, 1994.

G. Agnes
Associate Editor